GEOPHYSICS, VOL. 79, NO. 3 (MAY-JUNE 2014); P. WA107–WA115, 8 FIGS.
10.1190/GEO2013-0307.1

Data-driven wavefield focusing and imaging with multidimensional deconvolution: Numerical examples for reflection data with internal multiples

Filippo Broggini[1], Roel Snieder[2], and Kees Wapenaar[3]

ABSTRACT

Standard imaging techniques rely on the single scattering assumption. This requires that the recorded data do not include internal multiples, i.e., waves that have bounced multiple times between reflectors before reaching the receivers at the acquisition surface. When multiple reflections are present in the data, standard imaging algorithms incorrectly image them as ghost reflectors. These artifacts can mislead interpreters in locating potential hydrocarbon reservoirs. Recently, we introduced a new approach for retrieving the Green's function recorded at the acquisition surface due to a virtual source located at depth. We refer to this approach as *data-driven wavefield focusing*. Additionally, after applying source-receiver reciprocity, this approach allowed us to decompose the Green's function at a virtual receiver at depth in its downgoing and upgoing components. These wavefields were then used to create a ghost-free image of the medium with either crosscorrelation or multidimensional deconvolution, presenting an advantage over standard prestack migration. We tested the robustness of our approach when an erroneous background velocity model is used to estimate the first-arriving waves, which are a required input for the data-driven wavefield focusing process. We tested the new method with a numerical example based on a modification of the Amoco model.

INTRODUCTION

One of the main goals of exploration geophysics is to retrieve the location and amplitude of the discontinuities between structures with different properties within the subsurface from reflection data acquired at the surface of the earth. This is a challenging research task because an accurate image of the structures inside the earth is needed to locate energy sources, such as hydrocarbon reservoirs.

Standard imaging methods, such as one-way prestack migration (Claerbout, 1985) and reverse-time migration (RTM) (Baysal et al., 1983; McMechan, 1983), usually suffer from artifacts due to the presence of multiple reflections in the recorded data. We refer to these artifacts as ghost images, and they should not be confused with the water surface ghosts. These multiple reflections are often caused by high-impedance layers, such as salt bodies, and they can severely affect the final images. These imaging schemes, when applied to reflection data at the surface, cannot differentiate between primaries and multiples; hence, they erroneously interpret the multiply reflected waves as primary reflections due to deeper layers. This is the well-known single-scattering assumption (Oristaglio, 1989).

We have recently introduced a new method that allows us to retrieve the total wavefield (including all the internal multiples) originating from a point in the subsurface to receivers located at the surface (Wapenaar et al., 2012a, 2013). We refer to this approach as *data-driven wavefield focusing*. The Green's function is defined as the response recorded at the acquisition surface from a source located in the interior of the subsurface; see Figure 1b. Using source-receiver reciprocity, the Green's function can be interpreted as the response observed by a virtual receiver in the subsurface as a result of sources at the surface. The response at the virtual receiver is a combination of the downgoing and upgoing wavefields that are needed to reconstruct an image of the discontinuities inside the earth. The image built using this method will be free of internal multiple ghosts (Wapenaar et al., 2012b, 2014a). The downgoing and upgoing wavefields are illustrated in Figure 1c. The new method consists of an iterative algorithm that transforms the reflection response (at the acquisition surface) of an arbitrary lossless

Manuscript received by the Editor 14 August 2013; revised manuscript received 15 January 2014; published online 22 May 2014.
[1]Formerly Colorado School of Mines, Center for Wave Phenomena, Golden, Colorado, USA; presently ETH Zürich, Institute of Geophysics, Exploration and Environmental Geophysics, Zürich, Switzerland. E-mail: filippo.broggini@gmail.com.
[2]Colorado School of Mines, Center for Wave Phenomena, Golden, Colorado, USA. E-mail: rsnieder@mines.edu.
[3]Delft University of Technology, Department of Geoscience and Engineering, Delft, The Netherlands. E-mail: c.p.a.wapenaar@tudelft.nl.

medium into the wavefield generated by a virtual source inside the unknown medium. We assume that the reflection response at the surface is well sampled and that the free-surface multiples have been removed (Verschuur et al., 1992; Amundsen, 2001; Groenestijn and Verschuur, 2009). Apart from requiring the reflection data measured at the surface, data-driven wavefield focusing also requires an estimate of the traveltimes of the first-arriving wave traveling from the virtual source location to receivers located at the acquisition surface. These traveltimes, which could be computed using an eikonal solver in a background velocity model, are a key element of the method because they specify the location of the virtual source in the subsurface. Consequently, the proposed method is not model independent. However, we do not require any more knowledge of the medium parameters than standard primary imaging schemes and a smooth background velocity is usually sufficient. As in seismic interferometry (Curtis et al., 2006; Schuster, 2009), one of our goals is to retrieve the response to a virtual source inside an unknown medium and then use this response to build an image of the subsurface, hence, going beyond the single-scattering assumption. Moreover, our method is nonrecursive because we do not need to resolve the multiple problem in the overburden prior to imaging a specific deeper target zone. This means that it does not suffer from the error propagation that affects migration and full-waveform inversion.

We start with a brief review of the theory behind data-driven wavefield focusing and describe how to decompose the Green's function to its downgoing and upgoing components. Then, we apply the new method to a synthetic data set and compare its imaging capabilities with those of RTM. First, we create an image using crosscorrelation as the one-way imaging condition (Behura et al., 2012) and then we apply multidimensional deconvolution (MDD) (Wapenaar et al., 2008) to the decomposed wavefields to obtain an improved image. Finally, we show the robustness of our method when an erroneous velocity model is used to compute an estimate of the first-arriving waves.

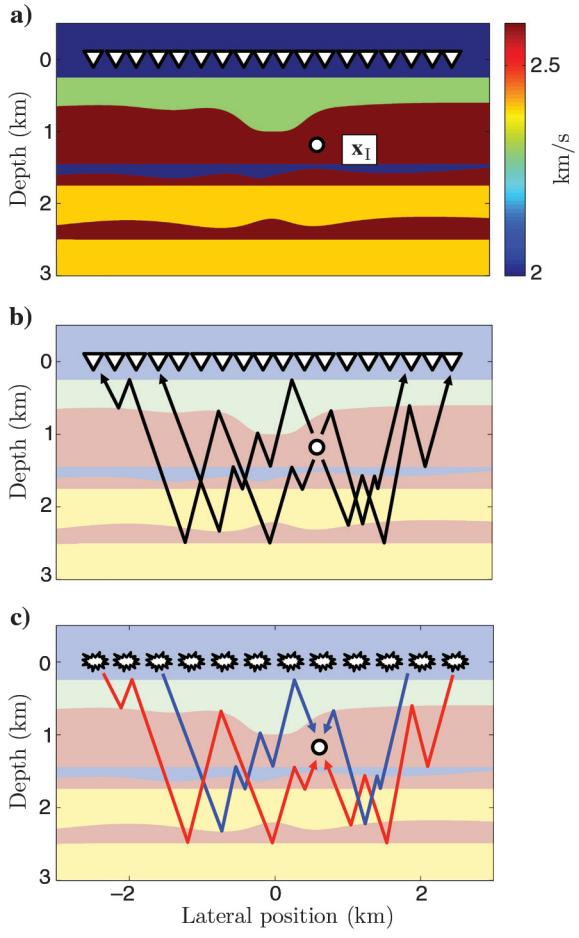

Figure 1. (a) Velocity model. (b) Rays corresponding to the total wavefield $G(\mathbf{x}_0, \mathbf{x}_I, t)$ from a virtual source at the imaging point located at $\mathbf{x}_I$ (indicated by the white dot) and recorded at the acquisition surface. The white circle indicates the location of the virtual source of the retrieved Green's function. (c) Decomposed wavefields. The solid blue rays correspond to the downgoing component $G^+(\mathbf{x}_I, \mathbf{x}_0, t)$. The solid red rays correspond to the upgoing component $G^-(\mathbf{x}_I, \mathbf{x}_0, t)$. The white circle indicates the location of the virtual receiver of the retrieved Green's function. In panels (b and c), the white triangles denote the receivers at $z = 0$ and the white explosions denote the sources at $z = 0$.

THEORY OF DATA-DRIVEN WAVEFIELD FOCUSING

Following recent work (Broggini et al., 2012; Wapenaar et al., 2012a), we briefly introduce the theory of data-driven wavefield focusing for 2D media and illustrate it with a numerical example in an inhomogeneous medium shown in Figure 1a. In a companion paper (Wapenaar et al., 2014a), we use a similar approach based on the 3D Marchenko equation. Furthermore, we have recently shown that these two approaches are equivalent (Wapenaar et al., 2013).

Our method implements an iterative scheme that requires (1) an estimate of the first-arriving wave between an image point $\mathbf{x}_I$ in the subsurface and the receivers at the surface and (2) the measured reflection response deconvolved for the source wavelet and without surface-related multiples. We denote these two inputs as $G_d(\mathbf{x}_0, \mathbf{x}_I, t)$ and $R(\mathbf{x}_0, \mathbf{x}, t)$, respectively. In the definition of the reflection response, $\mathbf{x}$ and $\mathbf{x}_0$ denote the source location and the receiver location, respectively. In case of multipathing, the first-arriving wave needs to include the corresponding triplications. If the estimate does not include such triplications, the retrieved wavefield also does not include the multiple paths. The first-arriving wave for the model of Figure 1a is shown in Figure 2. This is a particular case in which the direct arrival has no multipathing. The iterative scheme is based on a system of two equations that

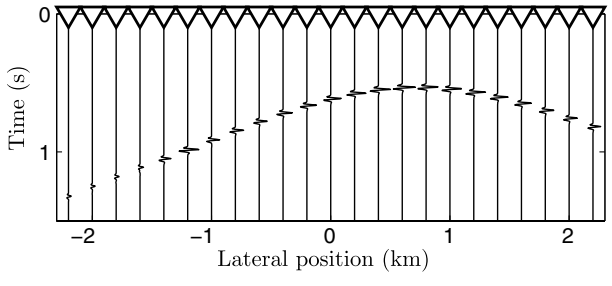

Figure 2. Estimate of the first-arriving wave propagating from image point $\mathbf{x}_I$ to the receivers (indicated by the white triangles) located at $z = 0$. The arrival times of this wave are denoted by $t_f(\mathbf{x}_0, \mathbf{x}_I)$, where $\mathbf{x}_0$ corresponds to the location of the receivers.

relates downgoing waves $p_k^+(\mathbf{x}_0, \mathbf{x}_I, t)$ and upgoing waves $p_k^-(\mathbf{x}_0, \mathbf{x}_I, t)$ at the acquisition surface $\partial\mathbb{D}_0$:

$$p_k^+(\mathbf{x}_0, \mathbf{x}_I, t) = p_0^+(\mathbf{x}_0, \mathbf{x}_I, t) - w(\mathbf{x}_0, -t)p_{k-1}^-(\mathbf{x}_0, \mathbf{x}_I, -t), \tag{1}$$

$$p_k^-(\mathbf{x}_0, \mathbf{x}_I, t) = \int_{\partial\mathbb{D}_0} R(\mathbf{x}_0, \mathbf{x}, t) * p_k^+(\mathbf{x}, \mathbf{x}_I, t)\mathrm{d}^2\mathbf{x}, \tag{2}$$

where k is the iteration number, $p_{-1}^-(\mathbf{x}_0, \mathbf{x}_I, t) = 0$, and the asterisk denotes temporal convolution. The window function $w(\mathbf{x}_0, t)$ satisfies

$$w(\mathbf{x}_0, -t) = \Theta(t + t_f(\mathbf{x}_0, \mathbf{x}_I) - \epsilon), \tag{3}$$

where $\Theta(t)$ is the Heaviside function, $t_f(\mathbf{x}_0, \mathbf{x}_I)$ is the arrival time of the first-arriving wave propagating from the target point $\mathbf{x}_I$ to the acquisition surface at $z = 0$, and ϵ is a small positive constant related to the duration of the source wavelet $s(t)$. In case of multipathing, $t_f(\mathbf{x}_0, \mathbf{x}_I)$ is the arrival time of the first onset of the triplicated wave. The window function $w(\mathbf{x}_0, -t)$ is equal to 1 for $t > -t_f(\mathbf{x}_0, \mathbf{x}_I) + \epsilon$ and equal to 0 elsewhere. The iterative scheme starts with the downgoing wavefield $p_0^+(\mathbf{x}_0, \mathbf{x}_I, t)$, which is defined as the time-reversed version of the first arriving wave, $G_d(\mathbf{x}_0, \mathbf{x}_I, -t)$, and it is only nonzero for $t < -(t_f(\mathbf{x}_0, \mathbf{x}_I) - \epsilon)$. Even though the method is iterative, an error (e.g., a time shift) introduced by $p_0^+(\mathbf{x}_0, \mathbf{x}_I, t)$ does not increase through the iterations because the same $p_0^+(\mathbf{x}_0, \mathbf{x}_I, t)$ is used in each iteration. The method converges after several iterations and we define the final results as p^+ and p^-, dropping the subscript k. The wavefields p^+ and p^- have a simple physical interpretation. The iterative scheme designs the downgoing wavefield p^+, which, when injected at the acquisition surface into the inhomogeneous medium, produces a focus at $t = 0$ at $\mathbf{x}_I$ (and at $\mathbf{x}_I$ only). The upgoing wavefield p^- is the response to p^+ measured at the same acquisition surface. Wapenaar et al. (2012a, 2013) show that the Green's function propagating between a location $\mathbf{x}_I$ within the subsurface and the receivers on the acquisition surface at $z = 0$ is related to the downgoing and upgoing wavefields p^+ and p^- by

$$G(\mathbf{x}_0, \mathbf{x}_I, t) = p^+(\mathbf{x}_0, \mathbf{x}_I, -t) + p^-(\mathbf{x}_0, \mathbf{x}_I, t). \tag{4}$$

The retrieved Green's function is shown in Figure 3a (in green), where it is superposed to the directly modeled reference wavefield (in black). The two wavefields match almost perfectly. A small mismatch is localized at a large offset and is denoted by the black arrow in Figure 3a. This mismatch is caused by the finite aperture of the employed receiver array and by refracted waves (such waves violate the up and down decomposition on which the theory is based). All traces have been multiplied by $\exp(2t)$ to emphasize the coda, which has been very well recovered. The number of iterations needed to reach convergence depends on the complexity of the subsurface. Wapenaar et al. (2012a) show that, for a simple medium, only one iteration is needed; whereas Broggini (2013) shows that the rate of convergence follows a geometric series. For this example, we performed 10 iterations. The iterative scheme we implement is equivalent to an integral equation that can be found by inserting equation 1 into equation 2 and dropping the subscript k (Wapenaar et al., 2012a). As an alternative to iteration, one could simply solve this integral equation.

Now, we apply a simple source-receiver reciprocity argument $G(\mathbf{x}_I, \mathbf{x}_0, t) = G(\mathbf{x}_0, \mathbf{x}_I, t)$ and define $G(\mathbf{x}_I, \mathbf{x}_0, t)$ as the wavefield originating from sources at the surface and observed by a virtual receiver located at the imaging point $\mathbf{x}_I$. To perform the decomposition of this Green's function in its downgoing $G^+(\mathbf{x}_I, \mathbf{x}_0, t)$ and upgoing $G^-(\mathbf{x}_I, \mathbf{x}_0, t)$ components, we consider a variant of the iterative scheme, in which the subtraction in equation 1 is replaced by an addition (Wapenaar et al., 2012b):

$$q_k^+(\mathbf{x}_0, \mathbf{x}_I, t) = q_0^+(\mathbf{x}_0, \mathbf{x}_I, t) + w(\mathbf{x}_0, -t)q_{k-1}^-(\mathbf{x}_0, \mathbf{x}_I, -t), \tag{5}$$

$$q_k^-(\mathbf{x}_0, \mathbf{x}_I, t) = \int_{\partial\mathbb{D}_0} R(\mathbf{x}_0, \mathbf{x}, t) * q_k^+(\mathbf{x}, \mathbf{x}_I, t)\mathrm{d}^2\mathbf{x}, \tag{6}$$

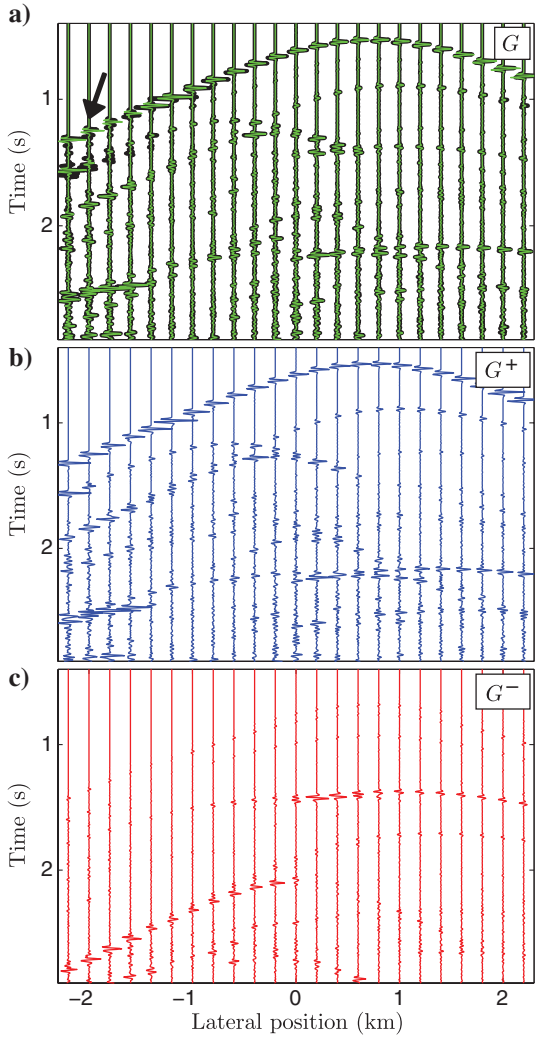

Figure 3. (a) Superposition of the reference wavefield $G(\mathbf{x}_0, \mathbf{x}_I, t)$ originated by a real source located at $\mathbf{x}_I$ (black line) and the wavefield retrieved by the iterative scheme (green line). The two wavefields match almost perfectly. The black arrow denotes a mismatch localizes at a large offset. (b) Downgoing wavefield $G^+(\mathbf{x}_I, \mathbf{x}_0, t)$. (c) Upgoing wavefield $G^-(\mathbf{x}_I, \mathbf{x}_0, t)$. All traces have been multiplied by $\exp(2t)$ to emphasize the scattering coda.

where the zeroth iteration of the downgoing field $q_0^+(\mathbf{x}_0, \mathbf{x}_I, t)$ is equal to $p_0^+(\mathbf{x}_0, \mathbf{x}_I, t)$ and $q_{-1}^-(\mathbf{x}_0, \mathbf{x}_I, t) = 0$.

After the second iterative scheme reaches convergence, we define two additional wavefields: $p_{\text{sym}}(\mathbf{x}_0,\mathbf{x}_I,t)=p(\mathbf{x}_0,\mathbf{x}_I,t)+p(\mathbf{x}_0,\mathbf{x}_I,-t)$ and $p_{\text{asym}}(\mathbf{x}_0, \mathbf{x}_I, t) = q(\mathbf{x}_0, \mathbf{x}_I, t) - q(\mathbf{x}_0, \mathbf{x}_I, -t)$ (Wapenaar et al., 2012b), where $p(\mathbf{x}_0, \mathbf{x}_I, t) = p^+(\mathbf{x}_0, \mathbf{x}_I, t) + p^-(\mathbf{x}_0, \mathbf{x}_I, t)$ and $q(\mathbf{x}_0, \mathbf{x}_I, t) = q^+(\mathbf{x}_0, \mathbf{x}_I, t) + q^-(\mathbf{x}_0, \mathbf{x}_I, t)$. The Green's function recorded at $\mathbf{x}_I$ is finally decomposed into downgoing and upgoing wavefields by combining $p_{\text{sym}}(\mathbf{x}_0, \mathbf{x}_I, t)$ and $p_{\text{asym}}(\mathbf{x}_0, \mathbf{x}_I, t)$ in two different ways, according to

$$G^+(\mathbf{x}_I, \mathbf{x}_0, t) = \frac{1}{2}\{p_{\text{sym}}(\mathbf{x}_0, \mathbf{x}_I, t) - p_{\text{asym}}(\mathbf{x}_0, \mathbf{x}_I, t)\}, \quad \text{for } t \geq 0, \tag{7}$$

and

$$G^-(\mathbf{x}_I, \mathbf{x}_0, t) = \frac{1}{2}\{p_{\text{sym}}(\mathbf{x}_0, \mathbf{x}_I, t) + p_{\text{asym}}(\mathbf{x}_0, \mathbf{x}_I, t)\}, \quad \text{for } t \geq 0. \tag{8}$$

These downgoing and upgoing (one-way) wavefields are used in the next section to create images of the subsurface with either crosscorrelation or MDD. Figure 3b–3c shows the decomposition of the total wavefield $G(\mathbf{x}_I, \mathbf{x}_0, t)$ of Figure 3a in its downgoing and upgoing components $G^+(\mathbf{x}_I, \mathbf{x}_0, t)$ and $G^-(\mathbf{x}_I, \mathbf{x}_0, t)$, respectively.

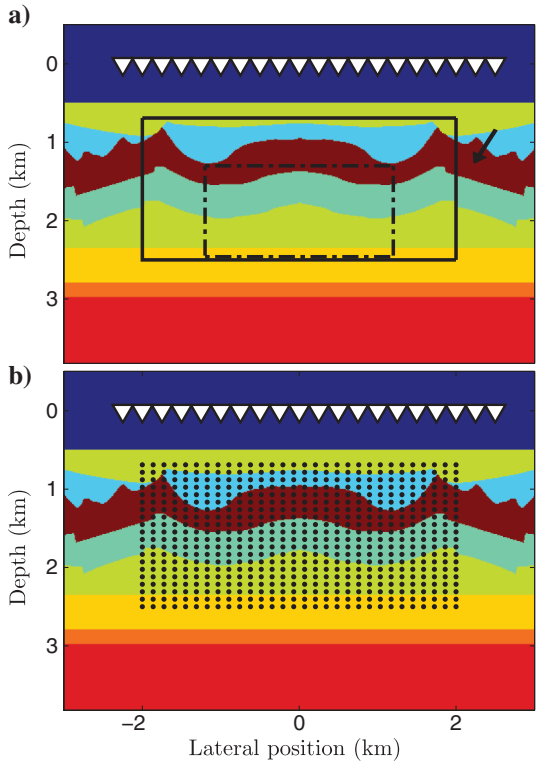

Figure 4. (a) Velocity model. The white triangles denote the receivers at $z = 0$. The black arrow indicates a layer characterized by higher impedance with respect to the surrounding layers. The solid rectangle encloses the target area used to compare the different imaging methods. The dashed rectangle bounds the portion of the subsurface used to compare the robustness of the different imaging methods when we use an erroneous background model. (b) The black dots correspond to various imaging points $\mathbf{x}_I$ used to build an image of the subsurface. Imaging points located on a constant depth level $z = z_i$ are used to resolve $[R(\mathbf{x}_r, \mathbf{x}, t)]_{z=z_i}$.

IMAGING

We consider a model based on a modified version of the Amoco data set, originally introduced by Etgen and Regone (1998), as shown in Figure 4a. Because our method allows for target-oriented imaging, we focus on the portion of the model enclosed by the solid rectangle in Figure 4a. The velocity and density profiles for this portion of the model are shown in Figure 5a and 5b. The black arrow in Figure 4a indicates a layer characterized by higher impedance with respect to the surrounding layers. This model is symmetric in the horizontal direction, which favors a visual comparison between the various images. However, the proposed iterative scheme is not restricted to a medium whose properties are symmetric in any particular direction.

We computed the response to 501 shots with sources located at $z = 0$ km. The acquisition surface is transparent; hence, no surface-related multiples are present. In the horizontal direction, the sources are located every 10 m between −2.5 and 2.5 km. In its current form, our method requires colocated sources and receivers. In practice, the required reflection responses are obtained from

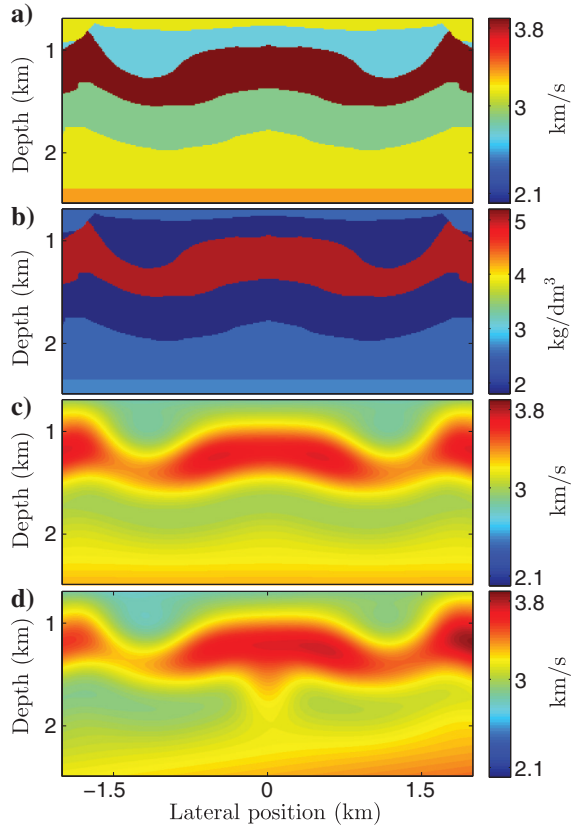

Figure 5. (a) Velocity model. (b) Density model. (c) Smooth background velocity model. (d) Erroneous background velocity model that presents a linearly increasing error in the horizontal direction from −6% to +6%, and a positive Gaussian anomaly centered at $\mathbf{x} = (0, 1.6)$ km.

conventional seismic reflection data after removal of the multiples due to the free-surface and deconvolution for the source wavelet (Verschuur et al., 1992; Amundsen, 2001; Groenestijn and Verschuur, 2009).

We compute the direct-arriving wavefront, the first input required by our method, using an eikonal solver. As an input for the solver, we use a smooth version of the velocity model; see Figure 5c. Note that, using an eikonal solver, we ignore the influence of the density. We introduce another approximation by assigning a constant amplitude to these first-arriving wavefields. This is done to reproduce the application of the method on real data when we only have an estimate of the background velocity of the subsurface and no information about the density. Alternatively, the direct arriving wavefront can be obtained by forward modeling in a macromodel, from microseismic events (Artman et al., 2010), from borehole check shots, or directly from the data by the common focus point (CFP) method (Berkhout, 1997; Thorbecke, 1997; Haffinger and Verschuur, 2012) when the imaging point is located at an interface.

Standard prestack imaging

For comparison, we start by computing a standard image using RTM (Baysal et al., 1983; McMechan, 1983; Biondi, 2006). RTM and many other seismic imaging algorithms rely on the single-scattering assumption. This implies that the recorded wavefields do not include internal multiples. When unwanted multiple reflections are present in the data, the imaging algorithm incorrectly images them as ghost reflectors. Our implementation of RTM uses a correlation imaging condition. However, in theory, other imaging conditions can be used (e.g., deconvolution, source-illumination normalized, etc.). This reference image is shown in Figure 6a, where we have used the same smooth model of Figure 5c needed to compute the first-arriving waves required by the iterative scheme. The high-impedance layer, indicated by the black arrow in Figure 4a, creates high-amplitude internal multiples. The white arrows in Figure 6a indicate some of the ghost reflectors present in this standard image. Additionally, the image is noisy below the high-impedance layer. The ghost reflectors and the noise partially mask the flat reflector at $z = 2.3$ km and affect the lateral continuity of the deeper reflectors. The black arrows indicate artifacts caused by multiply scattered waves. These waves are generated by the synclines located at the top of the high-impedance layer. The waves propagate downward, hit one of the deeply steeping walls of the synclines, propagate horizontally, bounce back on the other wall, and then travel back to the surface where they are recorded. Because of their multiple-scattering nature, these events are not handled correctly by the migration algorithm and are then imaged as artifacts located at larger depths with respect to the synclines.

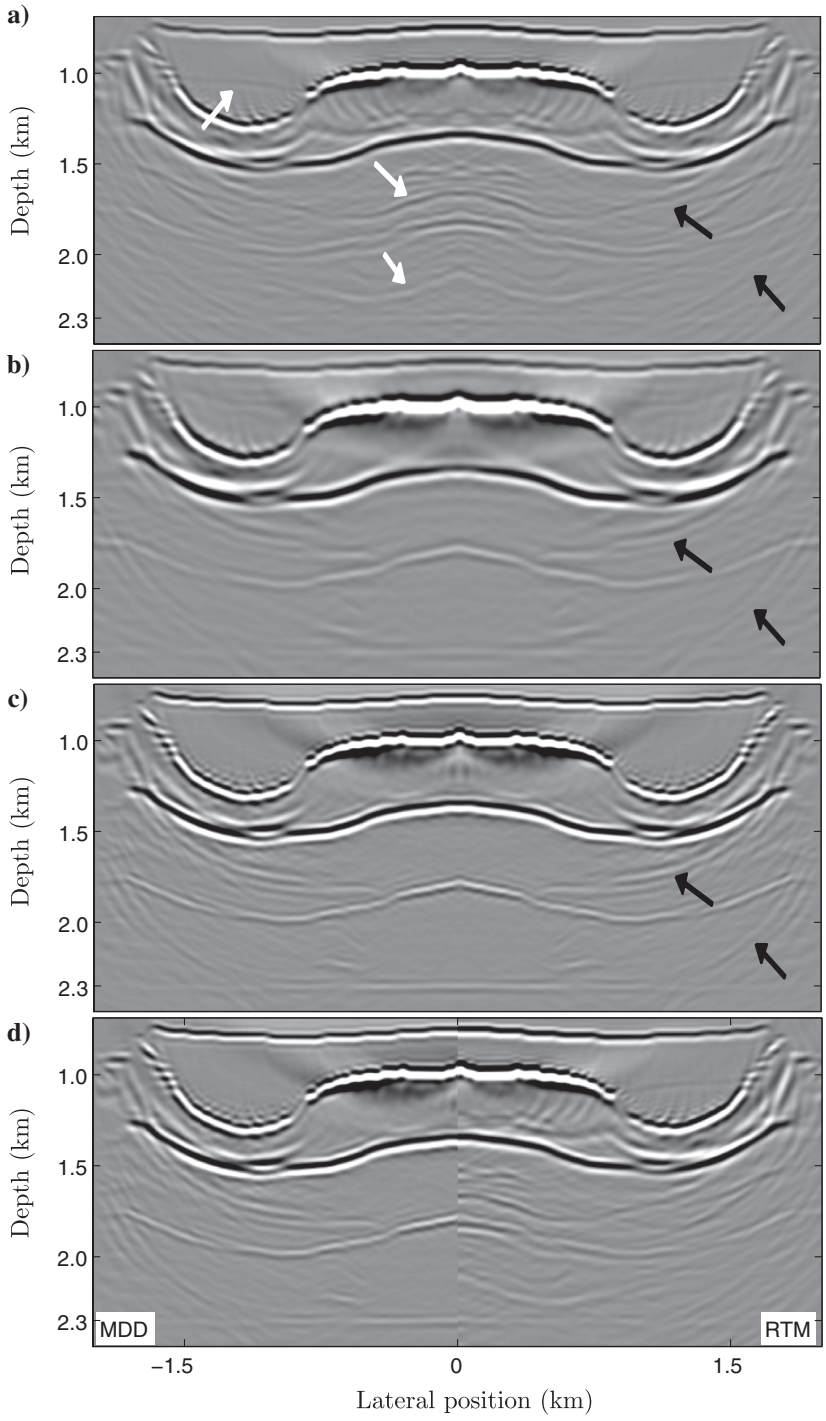

Figure 6. (a) Standard image of the reflectors obtained with RTM. The white arrows indicate some of the ghost reflectors present in the RTM image. (b) Image of the reflectors obtained with the crosscorrelation function C. (c) Image of the reflectors obtained with MDD. The black arrows indicate artifacts that have common features in the three different images. (d) Comparison between the standard image (right) and the one obtained with the combination of data-driven wavefield focusing and MDD (left).

Imaging with crosscorrelation

If we retrieve the Green's function with our method and decompose it into its downgoing and upgoing components, as described in the previous section, for image points $\mathbf{x}_\mathrm{I}$ located on many depth levels $z = z_i$ (e.g., the horizontal lines composed of black dots in Figure 4b), we are able to create a more accurate image of the medium. For this model, we perform 20 iterations to retrieve the Green's function at each imaging point. Following the steps in Behura et al. (2012), we compute the crosscorrelation function C,

$$C(\mathbf{x}_\mathrm{I}, \mathbf{x}_\mathrm{I}, t) = \int_{-\infty}^{\infty} G^{-}(\mathbf{x}_\mathrm{I}, \mathbf{x}_s, t) * G^{+}(\mathbf{x}_\mathrm{I}, \mathbf{x}_s, -t)\mathrm{d}x_s, \quad (9)$$

at every imaging point and evaluate the result at $t = 0$. The asterisk $*$ denotes temporal convolution, and $\mathbf{x}_s$ is located at $z = 0$. This new image is shown in Figure 6b. As in the reference image in Figure 6a, the actual reflectors have been reconstructed at the correct spatial location, but now the image is free of internal multiple ghosts. The image is less noisy, and the lateral continuity of the deeper reflectors is better preserved. This can be observed following the curved interface between 1.7 and 2 km, which is better defined when compared to the same interface in the RTM image shown in Figure 6a. This is an improvement over the previous image, but the amplitudes of the deeper targets, such as the flat reflector at $z = 2.3$ km that is still partially hidden, are not well retrieved. This is due to the facts that (1) we have a limited source aperture, (2) we do not take into account the multidimensional nature of the seismic wavefield, and (3) the reflectivity is the ratio of upgoing and downgoing waves that would require a deconvolution imaging condition rather than the standard crosscorrelation imaging condition. As in Figure 6a, the black arrows denote artifacts caused by horizontal propagating scattered waves. The theory behind our method (Wapenaar et al., 2014a, 2014b) is based on one-way propagation, where the preferred direction of propagation is the vertical one. For this reason, energy propagating along the horizontal direction is not properly handled by the data-driven wavefield focusing algorithm. This restriction only applies to the imaging depth level, where the decomposition takes place.

Imaging with MDD

MDD (Wapenaar et al., 2008) allows us to create an image with more accurate amplitudes. As in imaging with crosscorrelation, we consider a constant depth level $z = z_i$. The Green's functions at this constant depth level are related by

$$G^{-}(\mathbf{x}_r, \mathbf{x}_s, t) = \int_{-\infty}^{\infty} [R(\mathbf{x}_r, \mathbf{x}, t) * G^{+}(\mathbf{x}, \mathbf{x}_s, t)]_{z=z_i}\mathrm{d}x, \quad (10)$$

where $R(\mathbf{x}_r, \mathbf{x}, t)$ is the reflection response to downgoing waves at $z = z_i$ of the truncated medium below $z = z_i$, $\mathbf{x}_s$ is at $z = 0$, $\mathbf{x}_r$ is at $z = z_i$. The truncated medium is equal to the true medium below the depth level $z = z_i$ and is reflection-free above $z = z_i$. The reflectivity $R(\mathbf{x}_r, \mathbf{x}, t)$ can be resolved from equation 10 by MDD (Wapenaar et al., 2011). To achieve this result, we first correlate both sides of equation 10 with the downgoing Green's function and integrate over source locations over the acquisition surface:

$$C(\mathbf{x}_r, \mathbf{x}', t) = \int_{-\infty}^{\infty} [R(\mathbf{x}_r, \mathbf{x}, t) * \Gamma(\mathbf{x}, \mathbf{x}', t)]_{z=z_i}\mathrm{d}x,$$
$$\text{for } \mathbf{x}_r \text{ and } \mathbf{x}' \text{ at } z = z_i, \quad (11)$$

where C is the crosscorrelation function (as in the previous section, but with not-coinciding coordinates):

$$C(\mathbf{x}_r, \mathbf{x}', t) = \int_{-\infty}^{\infty} [G^{-}(\mathbf{x}_r, \mathbf{x}_s, t) * G^{+}(\mathbf{x}', \mathbf{x}_s, -t)]_{z_s=0}\mathrm{d}x_s, \quad (12)$$

and Γ is the point-spread function (van der Neut et al., 2011)

$$\Gamma(\mathbf{x}, \mathbf{x}', t) = \int_{-\infty}^{\infty} [G^{+}(\mathbf{x}, \mathbf{x}_s, t) * G^{+}(\mathbf{x}', \mathbf{x}_s, -t)]_{z_s=0}\mathrm{d}x_s. \quad (13)$$

We solve for $R(\mathbf{x}_r, \mathbf{x}, t)$ at different depth levels $z = z_i$ and many imaging points, as shown by the horizontal lines composed of black dots in Figure 4b, and evaluate the result at $t = 0$ and $x_r = x$. Figure 6c shows the final result of the imaging process. As in the previous image, the reflectors have been imaged at the correct spatial locations but now the relative amplitudes of the different reflectors are better retrieved. The flat reflector at $z = 2.3$ km is now more visible. Additionally, the lateral continuity of the deeper reflectors is still well preserved in comparison with the prestack image in Figure 6a. The black arrows denote artifacts that affect the image similarly to the one computed with crosscorrelation, as shown Figure 6b. The comparison between the standard image and the one obtained with the combination of data-driven wavefield focusing and MDD is shown in Figure 6d. MDD acknowledges the multidimensional nature of the seismic wavefield; hence, the internal multiples contribute to the restoration of the amplitudes of the reflectors. To improve the amplitudes of the standard prestack image, we could use an inversion-based imaging scheme such as least-squares migration (LSM) (Nemeth et al., 1999).

Vasconcelos et al. (2010) and Vasconcelos and Rickett (2013) use a similar approach to estimate the reflectivity operator $R(\mathbf{x}_r, \mathbf{x}, t)$, except that they need an accurate velocity model (which properly accounts for internal multiples) to depth-extrapolate fields, as opposed to upgoing and downgoing wavefields retrieved by data-driven wavefield focusing. Additionally, the wavefields retrieved with our approach can be used as input for recently developed nonlinear imaging methods (Fleury and Vasconcelos, 2012; Ravasi and Curtis, 2013).

Other existing methods aim at taking into account the internal multiples in the imaging process (Berkhout and Verschuur, 1997, 2011; Weglein et al., 1997; Jakubowicz, 1998; ten Kroode, 2002). However, similarities and differences with these methods need further investigation.

Imaging after redatuming of the reflection response

Alternatively, it is possible to take advantage of data-driven wavefield focusing to build an image of the subsurface without retrieving the decomposed wavefields at all the depth levels. For example, we choose a depth level below the high-impedance layer,

i.e., $z = 2.1$ km, and retrieve the downgoing and upgoing Green's functions only at this constant depth. Then, we apply MDD to retrieve the redatumed reflection response $R(\mathbf{x}_r, \mathbf{x}, t)$ at $z = 2.1$ km. This output is the reflection response that would be measured with sources and receivers located along a depth level at $z = 2.1$ km in a configuration with a homogeneous half-space above $z = 2.1$ km and equal to the true medium below the same depth level. The redatuming process removes the effect of the complex overburden from the reflection response (Sava and Biondi, 2004; Keho and Kelamis, 2012). We finally feed the redatumed reflection response in the RTM algorithm and this leads to the image shown in Figure 7a. The retrieved image correctly shows the three flat reflectors located between $z = 2.1$ and $z = 3.1$ km and is much less noisy than the reverse-time image computed using the reflection response recorded at the acquisition surface as shown in Figure 7b (this image is a close-up of Figure 6a). Both images have been computed using the smooth background velocity shown in Figure 5c. We discuss this methodology in more depth in a companion paper (Wapenaar et al., 2014a).

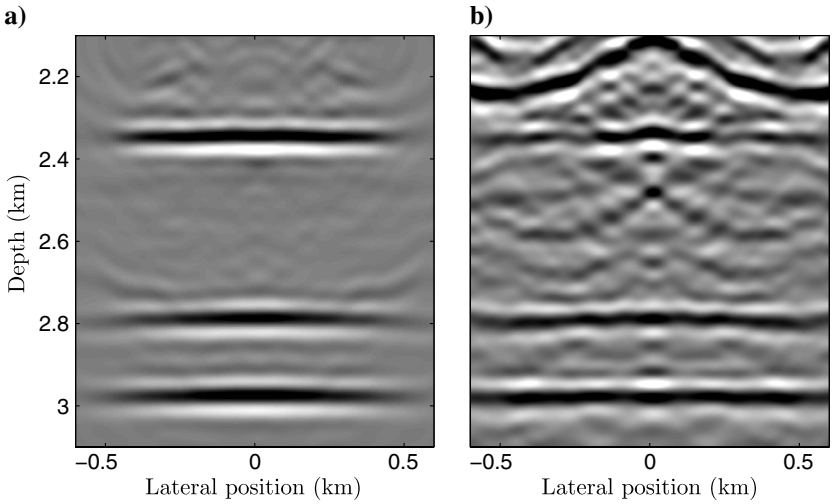

Figure 7. (a) Image of the three reflectors between $z = 2.1$ and $z = 3.1$ km obtained with RTM using as input the reflection response redatumed at $z = 2.1$. (b) Image of the reflectors obtained with standard prestack migration. This image is a close-up of Figure 6a. Both images have been computed using the smooth background velocity shown in Figure 5c.

Additionally, if we want to image a portion of the subsurface that is located between complicated overburden and underburden, we can take advantage of data-driven wavefield focusing to retrieve the reflection response from below (Wapenaar et al., 2014b). This allows us to illuminate our target area as if sources of seismic energy are placed below the target itself. In this particular situation, van der Neut et al. (2013) show how to combine the redatumed reflection response from above and below to perform *target-enclosing reflection imaging* of a target located between strongly scattering subsurface regions.

IMAGING WITH ERRONEOUS VELOCITY

We demonstrate the robustness of the combination of data-driven wavefield focusing and MDD when an erroneous velocity model is used to estimate the first-arriving waves (a required input for the focusing process). This numerical experiment is carried out with an erroneous background velocity that presents an error, linearly increasing in the horizontal direction from -6% to $+6\%$, and a positive Gaussian anomaly of $+10\%$ and width of 0.8 km centered at $\mathbf{x} = (0, 1.6)$ km, as shown in Figure 5d. Moreover, we compute a target-oriented image in a smaller portion of the model that is enclosed by the dashed rectangle in Figure 4a. We start by creating a standard image using RTM. This standard image is shown in Figure 8a, where we have used the erroneous background velocity model in the RTM algorithm. As expected, the reflectors are not symmetric in the horizontal direction. This is due to the part of the velocity error that varies linearly with x. Figure 8a shows that pronounced artifacts, such as ghost reflectors, affect the quality of the reference image. This image does not allow for a clear identification of the reflector at $z = 2.3$ km (which should now be imaged as a dipping reflector). This reflector does not appear to be any weaker or less focused than its counterpart in Figure 6a, but now the artifacts hide the lateral continuity of the reflector. The

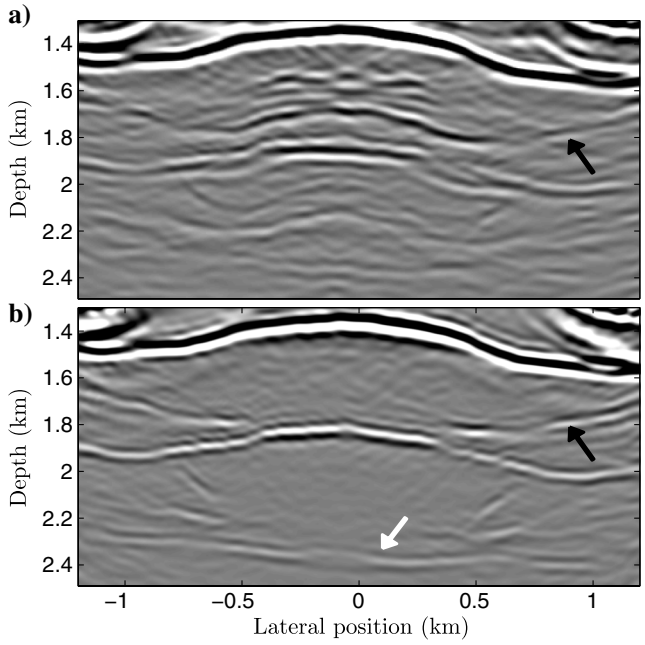

Figure 8. (a) Image of the reflectors obtained with standard prestack migration using a background velocity with an error, linearly increasing in the horizontal direction from -6% to $+6\%$, and a positive Gaussian anomaly of $+10\%$ and width of 0.8 km centered at $\mathbf{x} = (0, 1.6)$ km. The black arrow indicates an artifact due to a limited source aperture. (b) Image of the reflectors obtained with MDD. The first-arriving waves (a required input for the focusing process) are computed using the background velocity of Figure 5d. The black arrow indicates an artifact due to a limited-source aperture. The white arrow indicates the reflector at $z = 2.3$ km.

black arrow indicates a strong artifact consistent with the one present in Figure 6a–6c.

Figure 8b shows the result of MDD applied to the focused downgoing and upgoing wavefields. Similarly to the reference image, the reflectors have been reconstructed at the wrong spatial location (due to the erroneous background velocity), but now we obtain a superior image with fewer artifacts. Additionally, the image is less noisy and the reflector at $z = 2.3$ km, indicated by the white arrow in Figure 8b, is now more visible. The bump around $\mathbf{x} = (0, 2.3)$ km is due to the Gaussian anomaly centered at $\mathbf{x} = (0, 1.6)$ km. Note that the artifact indicated by the black arrow in Figure 8b is still present as in the image with correct background velocity, Figure 6c. This test shows that the image obtained by data-driven wavefield focusing (with an erroneous background model) still focuses the multiples along with the primaries, albeit at the wrong location. Moreover, the erroneous background model did not prevent the suppression of most of the multiple ghosts. Our method does not update the velocity model. However, we can use the redatumed reflection response to analyze some extensions of the image, such as angle gathers (Sava and Fomel, 2003) and subsurface offset gathers or time-lag gathers (Sava and Vasconcelos, 2011). Because the internal multiples are suppressed in these extended images, we envision that they are a suited starting point for updating the velocity model.

CONCLUSIONS

We showed that our recently introduced method for data-driven Green's function retrieval, allows us to construct an image that is not affected by ghost images of the reflectors. The retrieved downgoing and upgoing components of the Green's functions are the key components needed to obtain this result. These wavefields are then used to create different images of the medium with crosscorrelation and MDD. The images created with crosscorrelation and MDD show an improvement over standard imaging. Additionally, MDD yields an image whose amplitudes better agree with the correct reflection responses. This is due to the deconvolution process that correctly handles the internal multiples and retrieves more correct amplitudes of the primary reflections. We emphasize that, for the imaging with crosscorrelation and MDD, the imaging process does not require any more knowledge of the medium parameters than conventional imaging schemes based on primaries (which use a macromodel). However, the method requires a full acquisition geometry because the reflection response needs to be well sampled at the surface. Our method can be helpful in situations in which waves have traversed a strongly inhomogeneous and scattering overburden, e.g., subsalt and for near-surface imaging. In this particular situation, the decomposed wavefields could be used to perform target-enclosing reflection imaging of a salt body. The performance of the proposed method when strong multipathing of the direct arrival occurs is not addressed in this paper. Finally, the results in the last section of the paper show that data-driven wavefield focusing is robust with respect to errors in the background model used to estimate the first-arriving waves. The reflectors are as focused as in the standard prestack image, but the combination of data-driven wavefield focusing and MDD still removes the artifacts due to the presence of multiply scattered waves in the reflection data. This is a promising result toward future applications of the method on real data where we expect to have only estimates of the background velocity of the subsurface.

ACKNOWLEDGMENTS

This work was supported by the sponsors of the Consortium Project on Seismic Inverse Methods for Complex Structures at the Center for Wave Phenomena and the Netherlands Research Centre for Integrated Solid Earth Science (ISES). We thank E. Slob, J. Thorbecke, J. van der Neut (all at Delft University of Technology), and P. Sava (Center for Wave Phenomena) for useful discussions. F. Broggini is grateful to J. Behura for his collaboration. We are thankful to the associate editor B. Biondi, M. Ravasi, J. Rickett, and an anonymous reviewer for their constructive comments, which helped improve this paper. The reproducible numeric examples in this paper use the Madagascar open-source software package freely available from http://www.ahay.org.

REFERENCES

Amundsen, L., 2001, Elimination of freesurface related multiples without need of the source wavelet: Geophysics, **66**, 327–341, doi: 10.1190/1.1444912.

Artman, B., I. Podladtchikov, and B. Witten, 2010, Source location using time-reverse imaging: Geophysical Prospecting, **58**, 861–873, doi: 10.1111/j.1365-2478.2010.00911.x.

Baysal, E., D. D. Kosloff, and J. W. C. Sherwood, 1983, Reverse time migration: Geophysics, **48**, 1514–1524, doi: 10.1190/1.1441434.

Behura, J., K. Wapenaar, and R. Snieder, 2012, Newton-Marchenko-Rose imaging: 82nd Annual International Meeting, SEG, Expanded Abstracts, doi: 10.1190/segam2012-1531.1.

Berkhout, A. J., 1997, Pushing the limits of seismic imaging, Part I: Prestack migration in terms of double dynamic focusing: Geophysics, **62**, 937–953, doi: 10.1190/1.1444201.

Berkhout, A. J., and D. J. Verschuur, 1997, Estimation of multiple scattering by iterative inversion, Part I: Theoretical considerations: Geophysics, **62**, 1586–1595, doi: 10.1190/1.1444261.

Berkhout, A. J., and D. J. Verschuur, 2011, Full wavefield migration, utilizing surface and internal multiple scattering: 81st Annual International Meeting, SEG, Expanded Abstracts, 3212–3216.

Biondi, B., 2006, 3D seismic imaging: SEG.

Broggini, F., 2013, Wave field autofocusing and applications to multidimensional deconvolution and imaging with internal multiples: Ph.D. thesis, Colorado School of Mines.

Broggini, F., R. Snieder, and K. Wapenaar, 2012, Focusing the wavefield inside an unknown 1D medium — Beyond seismic interferometry: Geophysics, **77**, no. 5, A25–A28, doi: 10.1190/geo2012-0060.1.

Claerbout, J. F., 1985, Imaging the earth's interior: Blackwell Scientific Publications.

Curtis, A., P. Gerstoft, H. Sato, R. Snieder, and K. Wapenaar, 2006, Seismic interferometry — Turning noise into signal: The Leading Edge, **25**, 1082–1092, doi: 10.1190/1.2349814.

Etgen, J., and C. Regone, 1998, Strike shooting, dip shooting, widepatch shooting — Does prestack depth migration care? A model study: 68th Annual International Meeting, SEG, Expanded Abstracts, 66–69.

Fleury, C., and I. Vasconcelos, 2012, Imaging condition for nonlinear scattering-based imaging: Estimate of power loss in scattering: Geophysics, **77**, no. 1, S1–S18, doi: 10.1190/geo2011-0135.1.

Groenestijn, G. J. A. v., and D. J. Verschuur, 2009, Estimation of primaries and near-offset reconstruction by sparse inversion: Marine data applications: Geophysics, **74**, no. 6, R119–R128, doi: 10.1190/1.3213532.

Haffinger, P., and D. J. Verschuur, 2012, Estimation and application of near-surface full waveform redatuming operators: Geophysical Prospecting, **60**, 270–280, doi: 10.1111/j.1365-2478.2011.00983.x.

Jakubowicz, H., 1998, Wave equation prediction and removal of interbed multiples: 68th Annual International Meeting, SEG, Expanded Abstracts, 1527–1530.

Keho, T. H., and P. G. Kelamis, 2012, Focus on land seismic technology: The near-surface challenge: The Leading Edge, **31**, 62–68, doi: 10.1190/1.3679329.

McMechan, G. A., 1983, Migration by extrapolation of time-dependent boundary values: Geophysical Prospecting, **31**, 413–420, doi: 10.1111/j.1365-2478.1983.tb01060.x.

Nemeth, T., C. Wu, and G. T. Schuster, 1999, Least-squares migration of incomplete reflection data: Geophysics, **64**, 208–221, doi: 10.1190/1.1444517.

Oristaglio, M., 1989, An inverse scattering formula that uses all the data: Inverse Problems, **5**, 1097–1105, doi: 10.1088/0266-5611/5/6/015.

Ravasi, M., and A. Curtis, 2013, Nonlinear scattering based imaging in elastic media: Theory, theorems, and imaging conditions: Geophysics, **78**, no. 3, S137–S155, doi: 10.1190/geo2012-0286.1.

Sava, P., and B. Biondi, 2004, Wave-equation migration velocity analysis — II: Subsalt imaging example: Geophysical Prospecting, **52**, 607–623, doi: 10.1111/j.1365-2478.2004.00448.x.

Sava, P., and S. Fomel, 2003, Angle-domain common-image gathers by wavefield continuation methods: Geophysics, **68**, 1065–1074, doi: 10.1190/1.1581078.

Sava, P., and I. Vasconcelos, 2011, Extended imaging conditions for wave-equation migration: Geophysical Prospecting, **59**, 35–55, doi: 10.1111/j.1365-2478.2010.00888.x.

Schuster, G. T., 2009, Seismic interferometry: Cambridge University Press.

ten Kroode, F., 2002, Prediction of internal multiples: Wave Motion, **35**, 315–338, doi: 10.1016/S0165-2125(01)00109-3.

Thorbecke, J., 1997, Common focus point technology: Ph.D. thesis, Technische Universiteit Delft.

van der Neut, J., J. Thorbecke, K. Mehta, E. Slob, and K. Wapenaar, 2011, Controlled-source interferometric redatuming by crosscorrelation and multidimensional deconvolution in elastic media: Geophysics, **76**, no. 4, SA63–SA76, doi: 10.1190/1.3580633.

van der Neut, J., C. A. Vidal, N. Grobbe, and K. Wapenaar, 2013, Turning one-sided illumination into two-sided illumination by target-enclosing interferometric redatuming: 75th Annual International Conference and Exhibition, EAGE, Extended Abstracts, doi: 10.3997/2214-4609.20130190.

Vasconcelos, I., and J. Rickett, 2013, Broadband extended images by joint inversion of multiple blended wavefields: Geophysics, **78**, no. 2, WA147–WA158, doi: 10.1190/geo2012-0475.1.

Vasconcelos, I., P. Sava, and H. Douma, 2010, Nonlinear extended images via image-domain interferometry: Geophysics, **75**, no. 6, SA105–SA115, doi: 10.1190/1.3494083.

Verschuur, D. J., A. J. Berkhout, and C. P. A. Wapenaar, 1992, Adaptive surface-related multiple elimination: Geophysics, **57**, 1166–1177, doi: 10.1190/1.1443330.

Wapenaar, K., F. Broggini, E. Slob, and R. Snieder, 2013, Three-dimensional single-sided Marchenko inverse scattering, data-driven focusing, Green's function retrieval, and their mutual relations: Physical Review Letters, **110**, 084301, doi: 10.1103/PhysRevLett.110.084301.

Wapenaar, K., F. Broggini, and R. Snieder, 2012a, Creating a virtual source inside a medium from reflection data: Heuristic derivation and stationary-phase analysis: Geophysical Journal International, **190**, 1020–1024, doi: 10.1111/j.1365-246X.2012.05551.x.

Wapenaar, K., E. Slob, and R. Snieder, 2008, Seismic and electromagnetic controlled-source interferometry in dissipative media: Geophysical Prospecting, **56**, 419–434, doi: 10.1111/j.1365-2478.2007.00686.x.

Wapenaar, K., J. Thorbecke, J. van der Neut, F. Broggini, E. Slob, and R. Snieder, 2014a, Marchenko imaging: Geophysics, **79**, this issue, doi: 10.1190/geo2013-0302.1.

Wapenaar, K., J. Thorbecke, J. van der Neut, F. Broggini, E. Slob, and R. Snieder, 2014b, Green's function retrieval from reflection data, in absence of a receiver at the virtual source position: Journal of the Acoustical Society of America, doi: 10.1121/1.4869083.

Wapenaar, K., J. Thorbecke, J. van der Neut, E. Slob, F. Broggini, J. Behura, and R. Snieder, 2012b, Integrated migration and internal multiple elimination: 82nd Annual International Meeting, SEG, Expanded Abstracts, doi: 10.1190/segam2012-1298.1.

Wapenaar, K., J. van der Neut, E. Ruigrok, D. Draganov, J. Hunziker, E. Slob, J. Thorbecke, and R. Snieder, 2011, Seismic interferometry by crosscorrelation and by multi-dimensional deconvolution: A systematic comparison: Geophysical Journal International, **185**, 1335–1364, doi: 10.1111/j.1365-246X.2011.05007.x.

Weglein, A., F. Gasparotto, P. Carvalho, and R. Stolt, 1997, An inverse-scattering series method for attenuating multiples in seismic reflection data: Geophysics, **62**, 1975–1989, doi: 10.1190/1.1444298.